Supplementary Information file

Interfacing a nanostructured nickel oxide layer displaying fractal-like features with graphene: chemiresistive behaviour and GFET implementation

Michele Zanotti,[a] Elena Rolfi, [a,b] Sonia Freddi, [a,c] Stefania Pagliara,[a] Vincent Mazzola[d], Filiberto Ricciardella[d, e], Leandro Sacco[d] and Luigi Sangaletti [a]

a. Department of Mathematics and Physics, Università Cattolica del Sacro Cuore, via della Garzetta, 48 25133 Brescia (ITALY).
b. Present address: Department of Physics, Politecnico di Milano, P.le Leonardo da Vinci 32, 20131 Milan (Italy)
c. Institute of Photonics and Nanotechnologies - Consiglio Nazionale delle Ricerche (IFN-CNR), LNESS laboratory, Via Anzani 42, 22100 Como, Italy
d. VSParticle, Oostsingel 209, 2612HL Delft, The Netherlands.
e. Present affiliation: Quantum Technology Department, High Tech Industry, TNO, Stieltjesweg 1, 2628CK Delft, The Netherlands.

Optical and SEM microscopy analysis

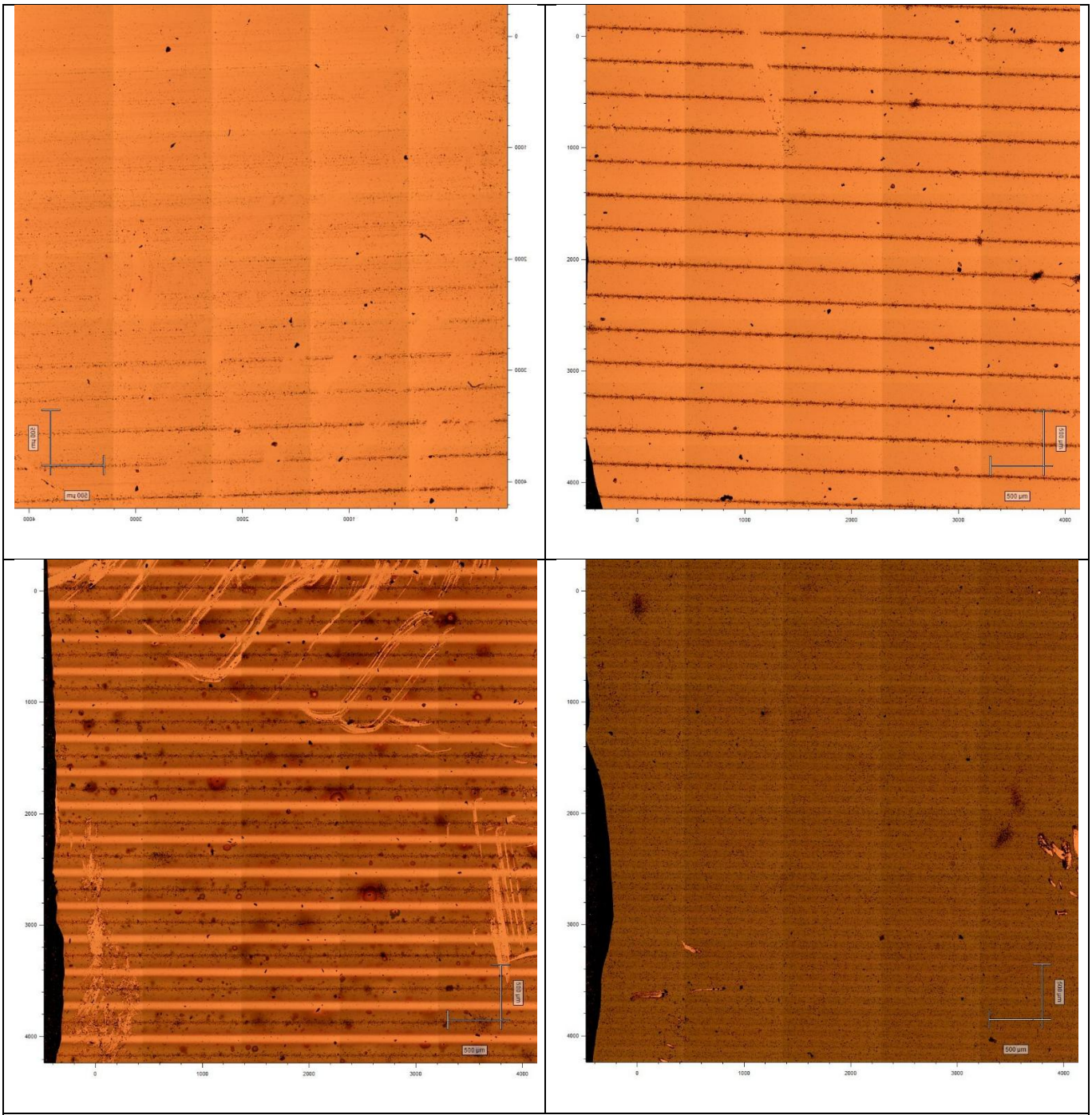

Figure S1. Optical images of the four samples. Left to right, top to bottom. S1, S2, S3, S4. Dark lines/areas: NiO; bright lines/areas: graphene. Dark stripes/lines are those covered by NiO_x nanoparticles. All images are produced by combining a grid of 5 x 8 smaller images. Vertical lines in all images are due to overlap between single images.

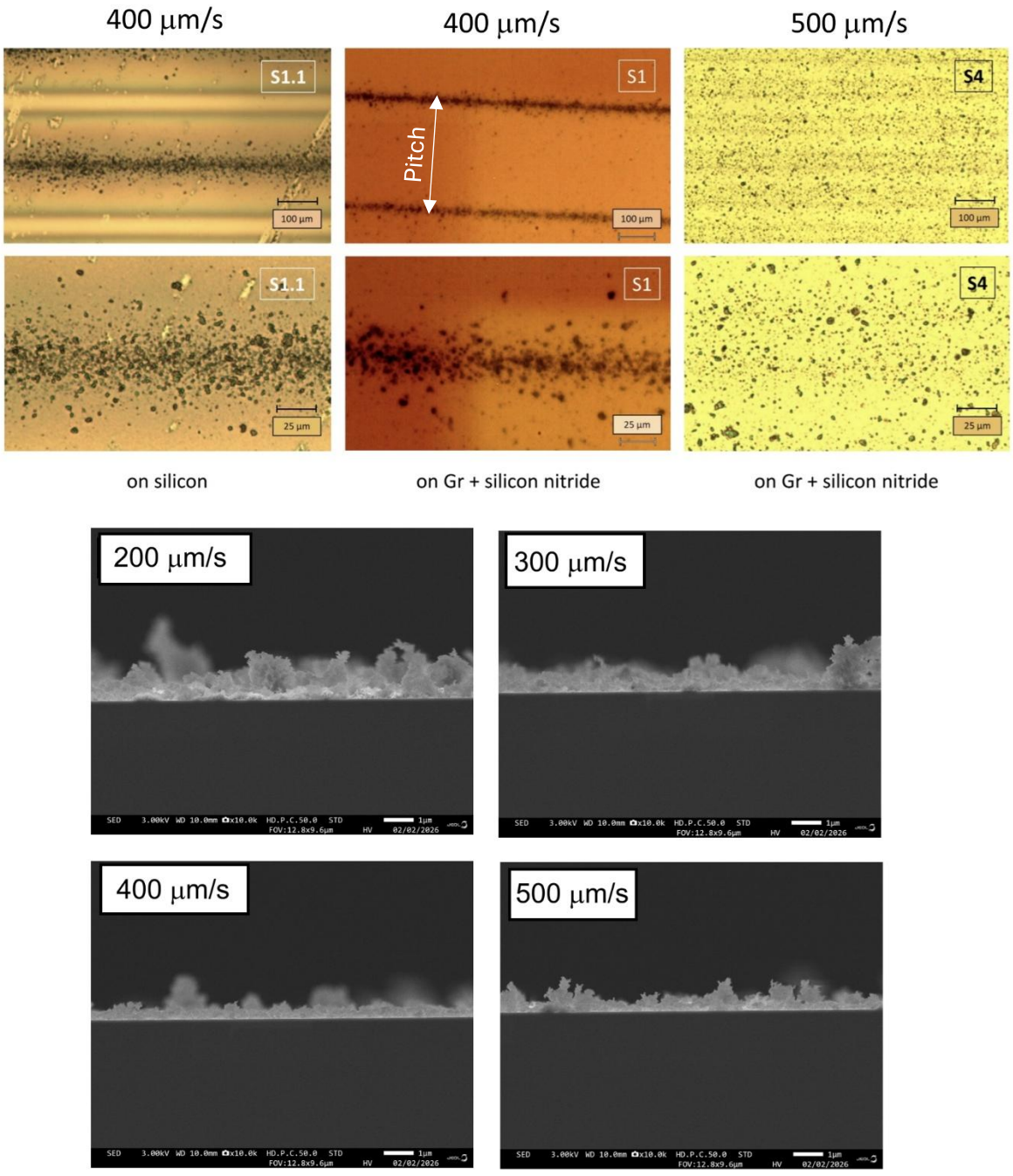

Figure S2. Top panel: details of optical imaging of samples S1, S4 and of sample S1.1, which was prepared by directly depositing the NP on a silicon wafer with the same parameters used for sample S1. The silicon wafer substrate of sample S1.1 provides a better optical contrast with respect to the Gr/Si_3N_4 substrate and the side bands of the central track became clearly visible. Pitch in sample S1.1 and S1 is 300 µm and the nozzle speed is 400 µm/s, while pitch in sample S4 is 50 µm and the nozzle speed is 500 µm/s. The reduced pitch with respect to the other samples produced in S4 a rather uniform layer with the largest thickness in the set, in spite of the smallest thickness of each single line. **Bottom panel**: cross-sectional SEM view of single lines deposited at increasing speed, from 200 µm/s to 500 µm/s.

Additional measurements on chemiresistive gas sensing.

Dynamical response to NH_3 from all samples.

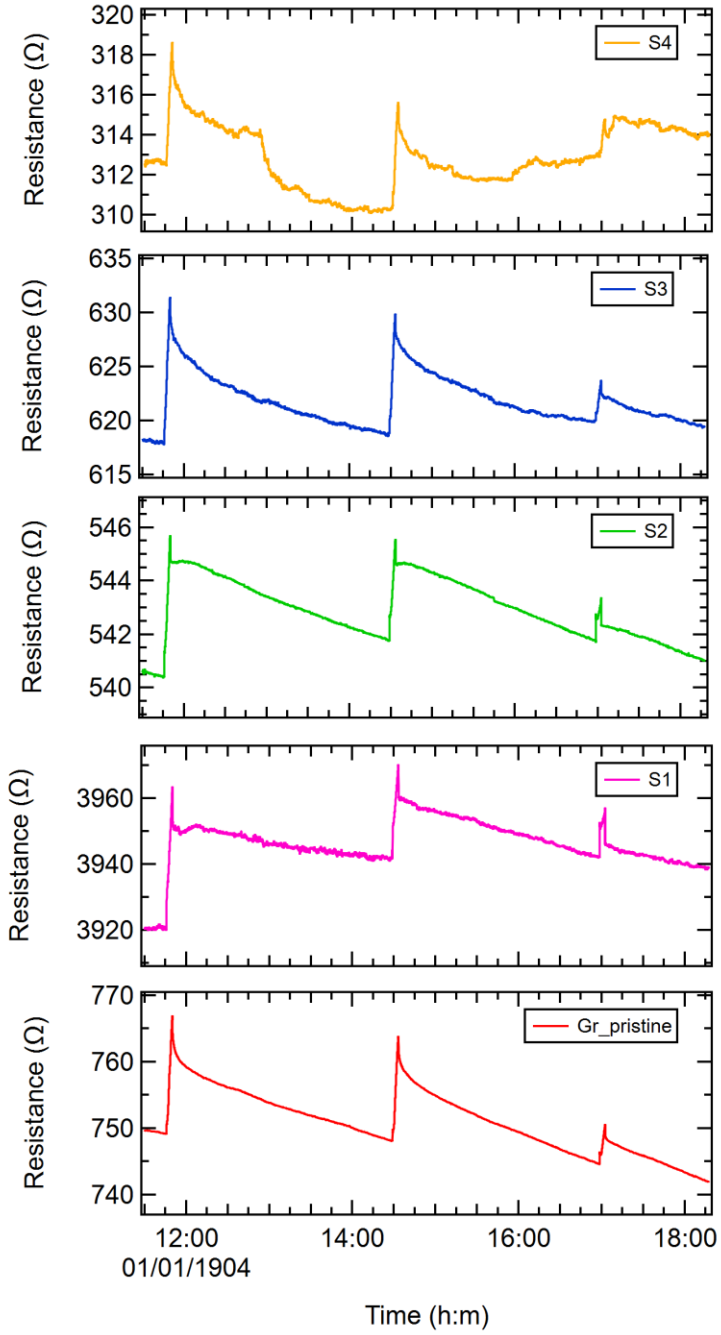

Figure S3. Example of dynamical response to NH_3 collected simultaneously by the 5 sensing layers in the lab environment. NH_3 concentration values: 17.8, 11.0, and 0.6 ppm (left to right). Relative humidity R.H.= 50%. Temperature = 23°C.

Table S1. Results of the calibration curve data fit with a Freundlich function: $\Delta R/R_0 = A$ [gas concentration]^{pow}

	Sample	**A x 10^{-3}**	**pow**
NH_3 (R.H. = 50%)	**S1**	2.9	0.43
	S2	2.1	0.50
	S3	5.5	0.48
	S4	4.0	0.55
	Gr	5.9	0.42
NO_2 (R.H. = 4%)	**S1**	-0.73	0.83
	S2	-0.43	0.96
	S3	-1.29	0.67
	S4	-	-
	Gr	-1.43	0.82

Response to NO_2 and NH_3 after 9 months

Table S2. Responses of the pristine graphene and S3 layers to NH_3 and NO_2. As prepared vs. aged samples.

sample	Analyte	Gas concentr.	RH (%)	Response X 10^{-3} [As prepared]	RH (%)	Response X 10^{-3} [After 9 months]
Pristine Gr	NH_3	25 ppm	50 ± 1	23 ± 2	4 ± 1	1.3 ± 0.1
S3	NH_3	25 ppm	50 ± 1	25 ± 2	4 ± 1	3.7 ± 0.4
Pristine Gr	NO_2	6 ppm	4 ± 1	6.4 ± 0.6	4 ± 1	9.0 ± 0.8
S3	NO_2	6 ppm	4 ± 1	4.2 ± 0.4	4 ± 1	5.0 ± 0.5

Batch-to-batch variation

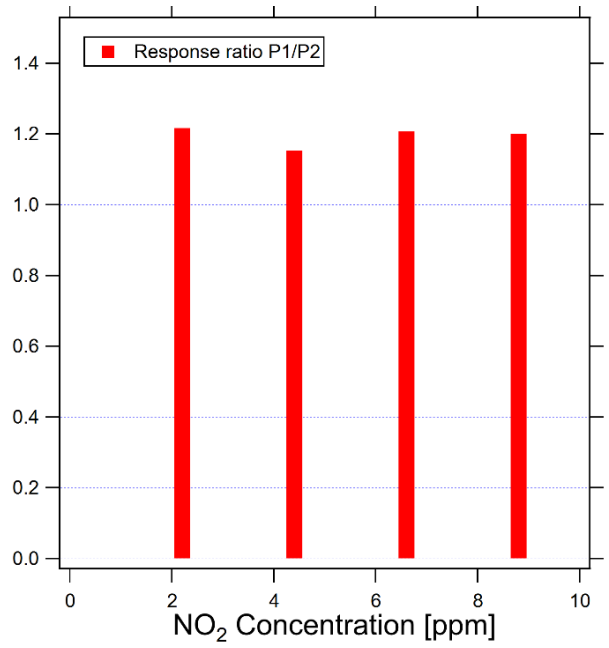

Figure S4. Comparison of the response to NO_2 at four different concentrations values for two pristine graphene layers (here labelled as P1 and P2) belonging to different batches. Each sample was extracted from a sealed box and both were promptly exposed to NO_2. The two sample batches were purchased three months apart and both were kept sealed until simultaneously opened. As can be observed a difference in the response of about 20% is observed, P1 dsplaying the highest response.

Calibration curves after 9 months

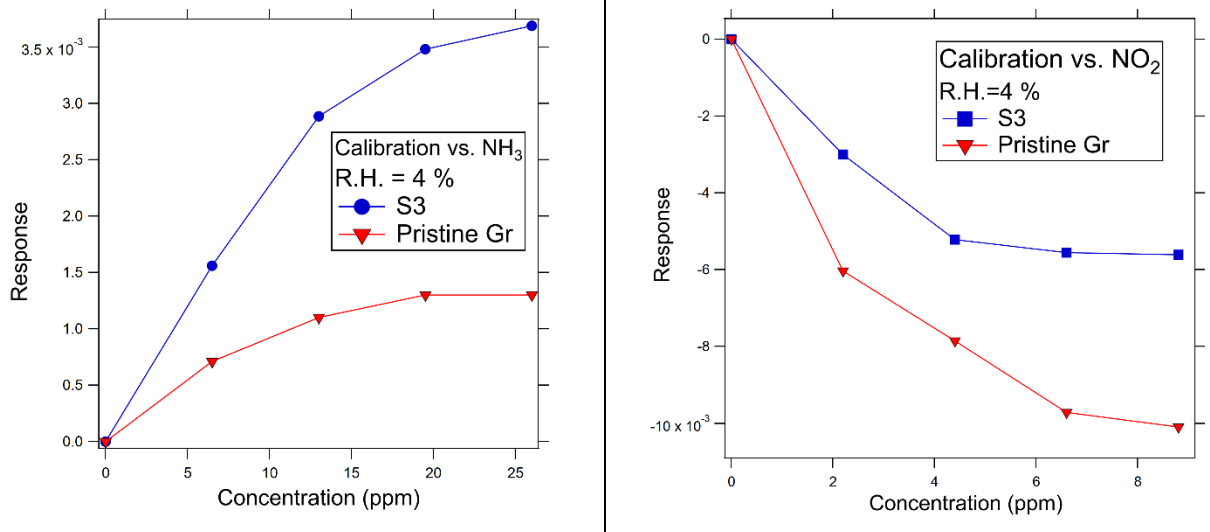

Figure S5. Calibration curves (i.e. response vs NH_3 or NO_2) for the pristine graphene and S3 samples. Lines are drawn as a guide for the eyes.

FE_SEM image analysis for fractal dimension estimation

Many nanostructured metal oxides (MOx) exhibit porous, self-similar, hierarchical structures that can be described using fractal models [**1-3**]. Self-similar, hierarchical architectures emerge in MOx synthesis and affect functional properties.

An analysis of fractal dimension and self-similarities in a representative sample was carried out, based on a set of eight FE-SEM images with magnification of 25x, 50x, 150x, and 300x (**Figure S6**). The following methods have been considered: Box-Counting Fractal Dimension Analysis, mean lacunarity **,** mean perimeter–area exponent, and Power Spectral Density Analysis.

The box-counting method overlays grids of varying sizes ε over a 2D image and counts occupied boxes to determine the fractal dimension. The analysis was carried out by overlaying a grid of boxes of size ε over each of the eight the FE-SEM images. Then the number of boxes $N(\varepsilon)$ that contain part of the structure was counted. This approach was repeated for smaller boxes sizes. From the slope of the linear region of the plot of log N(eps) vs. log (1/eps) the fractal dimension was obtained as:

$$\boldsymbol{D = \lim_{\varepsilon \to 0} \frac{\log N(\varepsilon)}{\log(1/\varepsilon)}}$$

The power spectral density analysis was considered to reveal self-similar properties through frequency domain characteristics. Starting from each FE_SEM image, the Fourier transfor of the signal was computed. The squared magnitude of the Fourier Transform gave the power at each frequency *f*. The plot of log (P(f)) vs. log(f) was obtained. The slope of the linear part of the plot indicates the scaling behavior, i.e. $P(f) \propto f^{-\beta}$.

Lacunarity analysis was carried out through the following steps. As first we created an overlay of the image (e.g. binary or grayscale) with a sliding box of size r. For each box the number of foreground pixels were counted. The quantity $\Lambda(r)$ was calculated according to the formula:

$$\Lambda(\boldsymbol{r}) = \frac{\boldsymbol{Variance(r)}}{[\boldsymbol{Mean(r)}]^{\boldsymbol{2}}} + \boldsymbol{1}$$

The slope in the log $\Lambda(r)$ vs. log r plot was the evaluated through a fitting of the $\Lambda(r)$ curve in the log-log scale. A negative slope means that lacunarity decreases with scale, indicating self-similarity.

The calculation of the mean perimeter-area is based on the identification in the FE-SEM image of shapes with perimeter P and area A. While for regular shapes (e.g. squares) in Euclidean geometry P scales as $A^{1/2}$, for irregular or fractal-like shapes, the perimeter grows faster with area and therefore P scales as $A^{D/2}$, with D>1. The D value can be retrieved from a log-log plot of the P vs. A curve.

Codes for the analysis of the FE-SEM images were written in the Python programming language. From the analysis of the eight images, the following results were obtained. The average fractal dimension obtained via **box-counting** is D = 2.01, with a coefficient of determination $R^2 > 0.99$, providing strong evidence of self-similar behavior. The **mean lacunarity** slope is –0.52,

indicating a non-random and heterogeneous distribution of voids. The **mean perimeter–area exponent**, D = 1.18, reflects the presence of highly irregular and complex boundaries. According to the theory of self-affine fractal surfaces in two dimensions **[4]** $D_{(Fourier)} = (7-\beta)/2$, therefore the **spectral exponent** $\beta = 3.24$, corresponds to a Fourier fractal dimension of $D_{(Fourier)} = 2.62$. **Figure S7**, displays a typical outcome of the four methods referred to a single image. Taken together, these four independent analyses converge to support the presence of robust fractal characteristics across the 15–500 nm spatial scale. Data from individual images analysis are reported in **Table S3**.

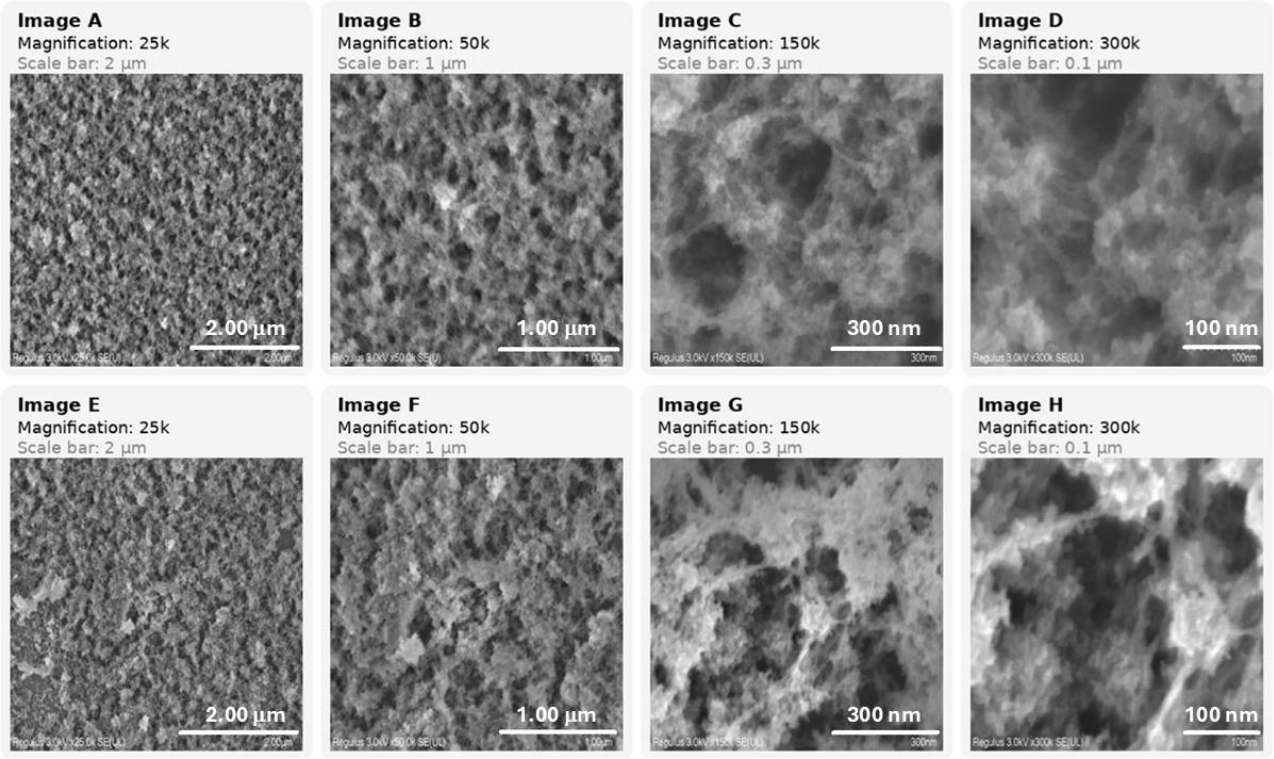

Figure S6. FE-SEM images taken over two distinct points of the sample with four magnification (25K, 50K, 150K, 300K) each.

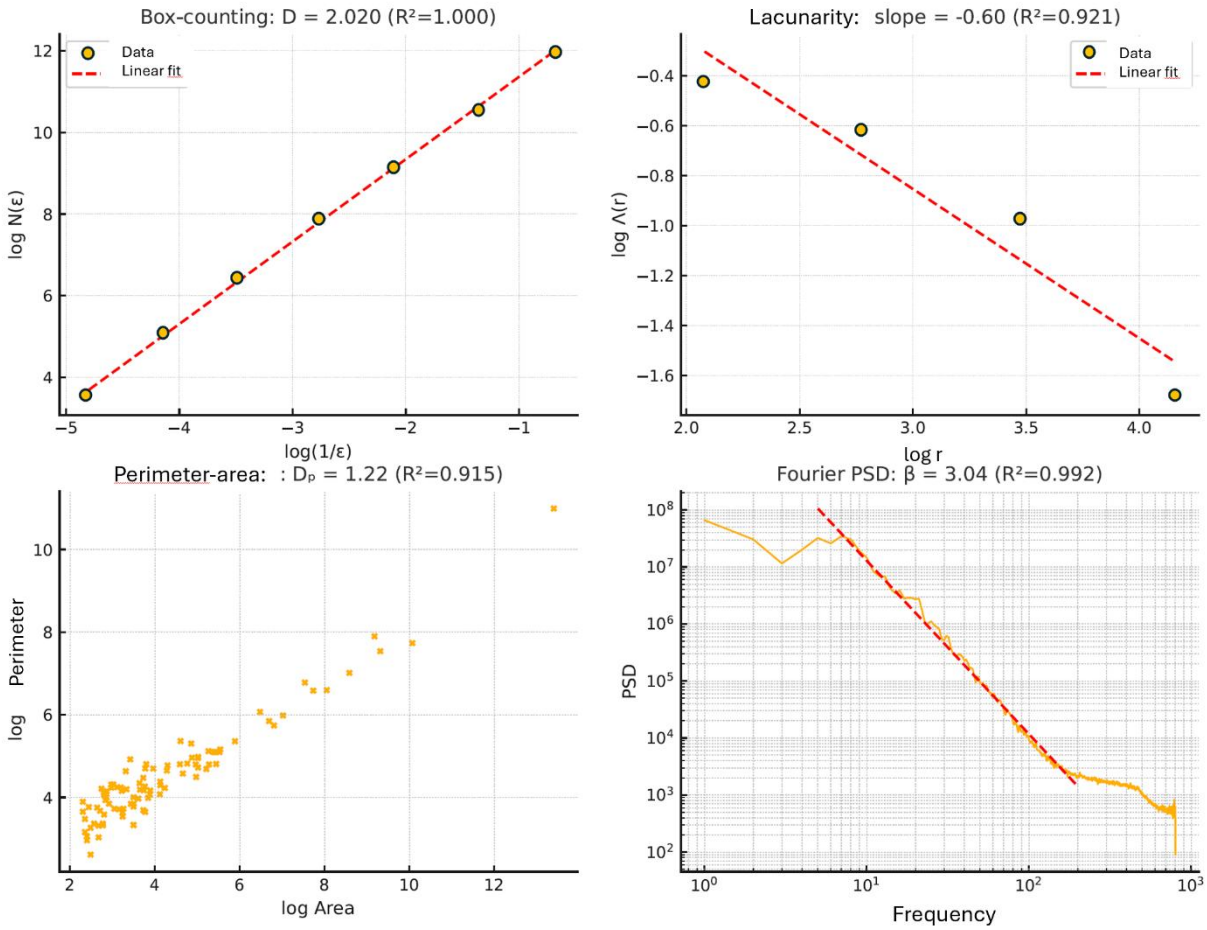

Figure S7. Example of FE-SEM images data analysis outcome based on the four methods adopted: Box-Counting, Lacunarity, Perimeter-area, PSD. Results are summarized in Table S1, image 3.png.

Table S3. Results of the fractal dimension analysis carried out over the eight panels (FE-SEM images) of Figure S1. Imagine label, box-counting dimensionality D_box, R^2 coeffcient on D_box, Lacunarity analysis slope Lac_slope, R^2 of Lac_slope, mean perimeter-area exponent D_perim, R^2 on D_perim, β coefficient of PSD, R^2 on β.

Imagine	D_box	R^2_box	Lac_slope	R^2_lac	D_perim	R^2_perim	β	R^2_PSD
1.png	2.015	0.999	-1.151	0.940	1.276	0.942	2.841	0.933
2.png	1.990	1.000	-0.230	0.944	1.101	0.856	3.463	0.991
3.png	2.020	1.000	-0.598	0.921	1.218	0.915	3.041	0.992
4.png	2.056	0.999	-0.146	0.930	1.037	0.858	3.242	0.965
5.png	1.994	1.000	-1.036	0.950	1.293	0.953	2.656	0.953
6.png	1.984	1.000	-0.586	0.945	1.164	0.942	3.474	0.976
7.png	2.021	1.000	-0.211	0.950	1.162	0.876	3.734	0.991
8.png	1.986	1.000	-0.172	0.926	1.156	0.890	3.491	0.967

Additional Raman spectroscopy data

Full Raman data in the 1200-3200 cm^{-1} range are shown in **Fig. S8**. In addition to the G Band (at approx. 1580 cm^{-1}) and 2D Band (at approx. 2680 cm^{-1}), a weak contribution from the D band is detectable as a broad feature aboe 1300 cm^{-1}. Furthermore, in all samples a series of sharp peaks, labeled with diamonds in the Figure, appear in the 1340–1530 range. These are identified at the following Raman shifts (1340 cm^{-1} ; 1445 cm^{-1} ; 1530 cm^{-1}). The peak at 1340 cm^{-1} occupies the same spectral region as the graphene D-band (defect-induced breathing mode). However, the concomitant appearance of the 1445 cm^{-1} and 1530 cm^{-1} peaks suggests a non-intrinsic origin. We rule out PMMA contaminations **[5]** from the Gr to Si_3N_4 transfer process, as they display much broader and more intense bands in other spectral regions (about 3000 cm^{-1}) where we do not detect Raman signal.

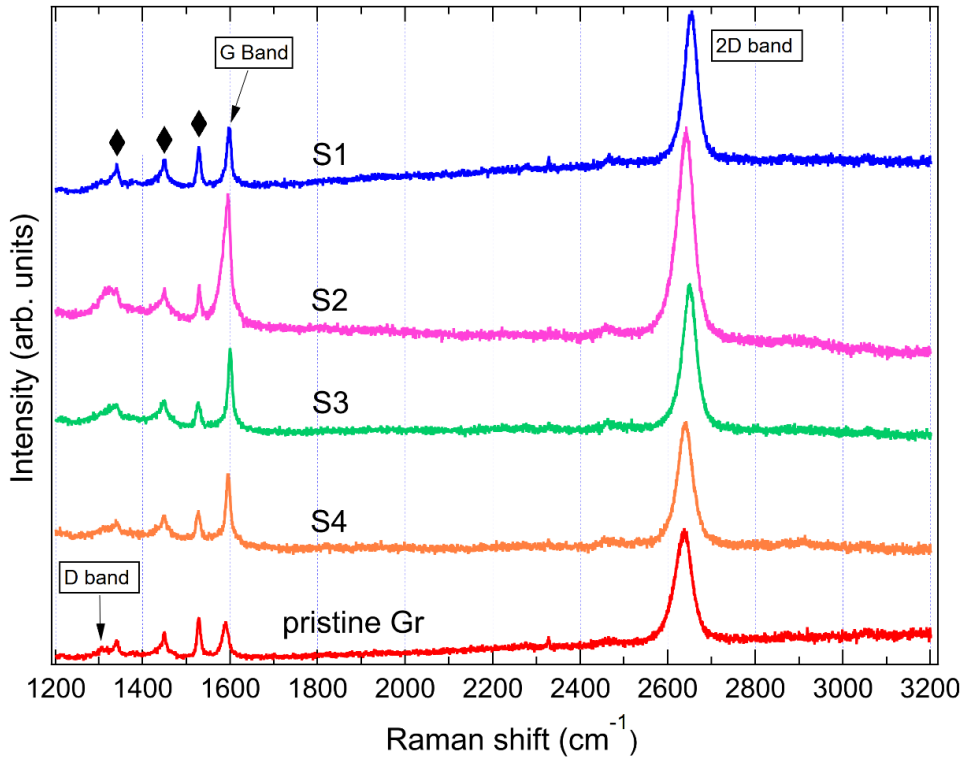

Figure S8. Extended Raman spectra of the 5 samples in the 1200-3200 cm^{-1} range. Spectra have been collected with a 100x objective (N.A. = 0.9) of a microRaman equipped with a 633 nm He-Ne laser.

Analysis of interference effects due to the Si_3N_4 buffer layer

Due to the stack of layers for the present sample, we argue first that interference effects needs to be considered to properly weight the peak intensities. Following **Ref.[6]**, multiple reflection calculations have been carried out, by properly considering the laser wavelength, the Si_3N_4 layer

thickness, and the objective of the micoRaman probe. The results of multiple-reflection field enhancement are shown in **Fig.S9 and Fig.S10** below. As can be observed, while the field at the Gr surface is much reduced, its maximum is found in the bulk of the Si_3N_4 layer (i.e., at 70-80 nm, depending on the laser wavelength).

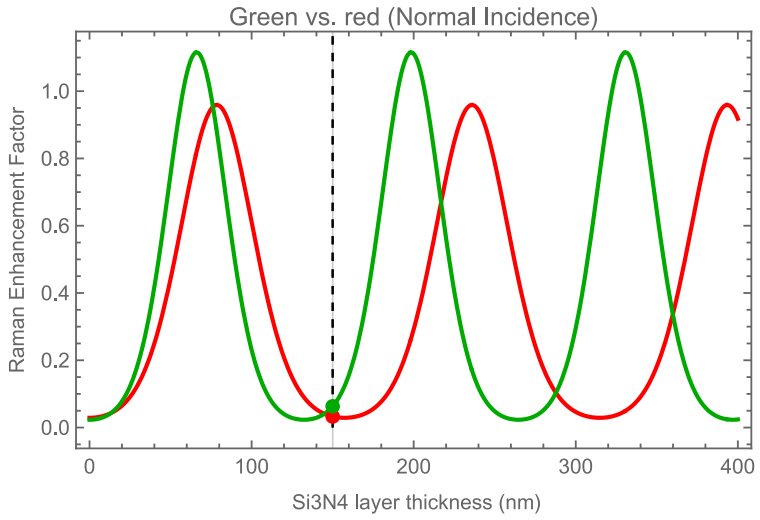

Figure S9. Raman enhancement factor due to interference effects through a Si_3N_4 layer for a laser beam with λ=633 nm (red) and λ=532 nm (green).

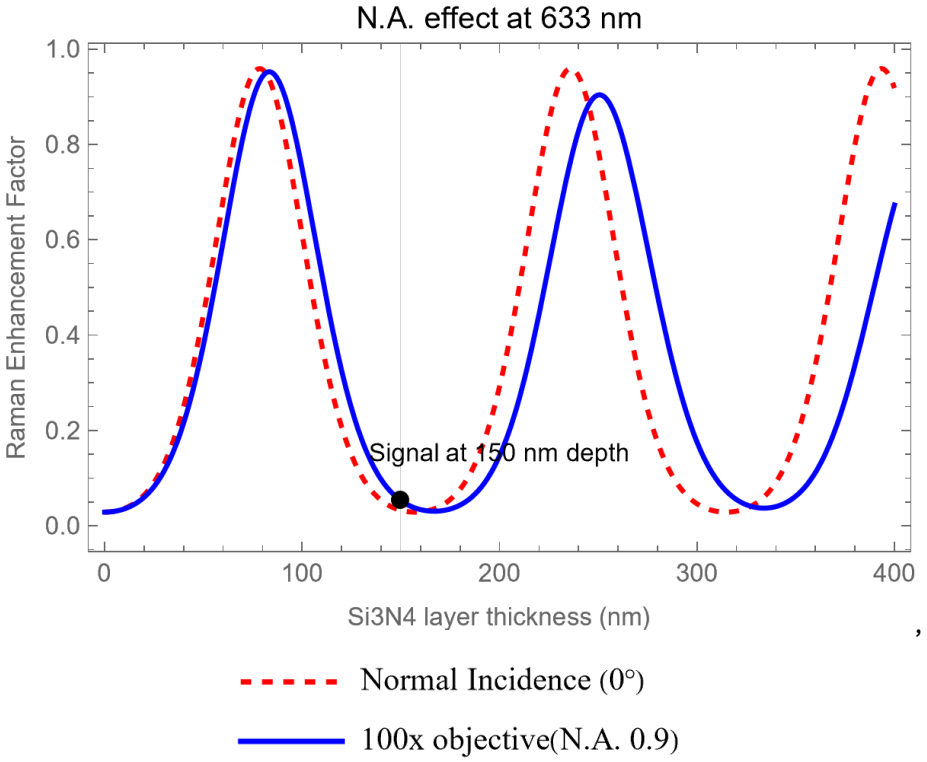

Figure S10. Simulation of Raman enhancement in the case of normal-incidence laser beam (λ=633 nm) without any lensing system (dashed line) and in case a 100x objective (numerical aperture N.A. = 0.9) of an optical microscope is used to focus the beam and collect the scattered light.

Therefore the three bands at 1340 cm^{-1} ; 1445 cm^{-1} ; 1530 cm^{-1} can be ascribed to an enhancement of Raman scattering within the Si_3N_4 layer, thereby excluding possible surface contaminations at the graphene surface of GR- Si_3N_4 interface. This suggests that they can be ascribed to impurities trapped in the CVD grown Si_3N_4 layer.

The 150 nm Si_3N_4 layer acts as an optical interference cavity. This specific substrate thickness facilitates constructive interference of both the excitation laser and the backscattered Raman light. This mechanism can selectively amplify or quench signals from selected depth across the sample, depending on the position of nodes of the field standing waves.

In this frame, the high relative intensity of the substrate peaks—approaching the magnitude of the G-band in some spectra—is not indicative of high impurity concentrations, but rather a result of selective enhancement. Finally, in our devices Si_3N_4 plays the role to decouple Gr from Si and avoid any leakage current through the doped-Si wafer substrate. For this reason neither Si_3N_4 nor impurities inside it are effective in the sensing mechanism.

XPS analysis and fitting of selected C 1s core level data

In order to fit the C 1s XPS peaks and identify the different contributions to this core line, we considered all possible components detailed in a review paper by Chen et al. **[7]**. In addition, we considered the peak at BE lower than the sp^2 carbon peak of graphene, following the analysis of **Blume et al. [8]**. We assume that C sp^3 contribution in the C 1s XPS spectrum is quite low, as we see a low-intensity D peak in the Raman spectra of all samples, being the D band usually ascribed to sp^3 carbon defects. The binding energy ranges reported in Ref.[7] for graphene are: C=C (284.3–284.6 eV), C–C (284.9–285.6 eV), C–OH (285.4-286.7 eV), C–O–C (285.6-286.9 eV), C=O (287.9-288.3 eV), and COOH/COOR (288.3–289.4 eV). The C 1s spectra that we present in **Fig. S11** were fitted with up to 5 gaussian peaks, and these peaks were ascribed to:

- defected C, peak 0
- C=C (284.3–284.6 eV) C sp^2, peak 1
- C–C (284.9–285.6 eV) C sp^3, peak 2
- C–OH (285.4-286.7 eV), C–O–C (285.6-286.9 eV), peak 3
- COOH/COO-R (288.3–289.4 eV). Peak 4

In **Fig. S11** the C 1s XPS spectra from the pristine graphene sample, from the S3 layer, and from the pristine graphene sample after annealing in ultra-high vacuum conditions are shown. This annealing is used to induce desorption of contaminants from the graphene layer. During the annealing, the sample temperature slowly increased up to 500°C. The total annealing time was 70 minutes. As can be observed, after annealing in UHV the peaks 3 and 4, ascribed to the presence of oxygen related species is much reduced, indicating and extrinsic origin of these contaminations. However, we need to keep in mind that these species are found on the surface as soon as it is exposed ambient air. Therefore, the C 1s XPS peak is representative of the Gr layer just before being exposed to the analytes. As for sample S3, we observe the features at high BEs already detected for pristine graphene. Their intensity looks a bit higher with respect of the pristine graphene case and therefore we assume that the presence of the nanostructured NiO overlayer can getter extra oxygen-related contaminations form the ambient air. Finally, in sample S3 we can clearly detect peak 0, which is

ascribed to defects in the C layer, as recognized in Ref. **[8]**. The relative weight of the various components of C 1s we have identified is detailed in **Table S4**.

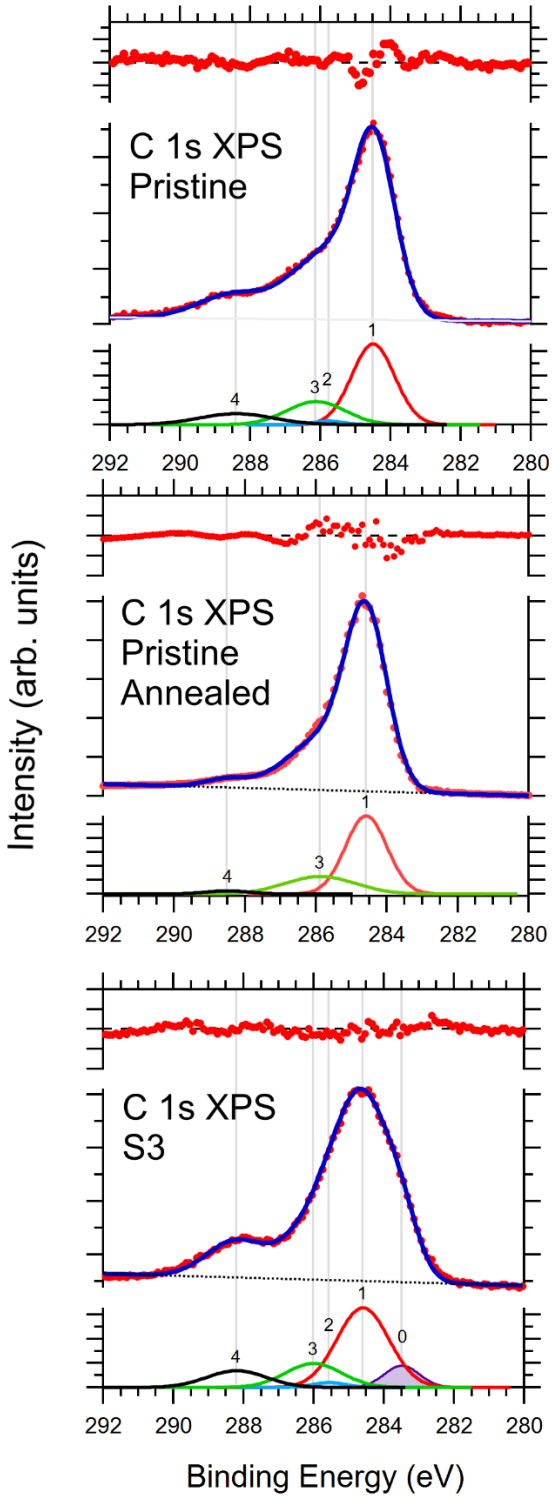

Figure S11. C 1s XPS spectra of pristine graphene (top panel), annealed pristine graphene (middle panel), and S3 (bottom panel) samples. Spectra were fitted with up to five gaussian peaks labelled as Peak 0 (defected carbon), Peak 1 (C sp^2 from graphene), Peak 2 (carbon sp^3), Peak 3 (C–OH and C–O–C), and Peak 4 (COOH/COO-R), in order of increasing binding energies.

Table S4. Fitting results of the C 1s XPS peak for the annealed, pristine and S3 samples. Relative weight (%) of the 5 peaks considered in the fitting. Error bar = ± 1.5 %. Data taken from Figure S11. Peak 0 (defected carbon), Peak 1 (C sp^2 from graphene), Peak 2 (carbon sp^3), Peak 3 (C–OH and C–O–C), and Peak 4 (COOH/COO-R).

	Peak 0	Peak 1	Peak 2	Peak 3	Peak 4
Annealed	0.0	74.7	0.0	21.5	3.7
Pristine	0.0	68.1	3.1	19.5	9.3
S3	14.8	54.3	3.3	16.3	11.3

References

1. P. Meakin. *A historical introduction to computer models for fractal aggregates*. *Journal of Sol-Gel Science and Technology*, (1999) **15**, 97

2. P. Pfeifer and D. Avnir, *Chemistry in noninteger dimensions between two and three. I. Fractal theory of heterogeneous surfaces*. The Journal of Chemical Physics (1983) **79**, 3558.

3. M.A. Aegerter, N. Leventis (Eds.) Aerogels Handbook. Springer, 2011.

4. J.C. Russ, Fractal Surfaces, Springer, 1994.

5. E.V. Barmina, N.N. Mel'nik, I.I. Rakov, G.A. Shafeev, *Optical properties of nanocomposites based on polymers and metal nanoparticles*, Physics of Wave Phen. (2017), **25**, 165–169.

6. D. Yoon, H. Moon, Young-Woo Son, Jin Sik Choi, Bae Ho Park, Young Hun Cha, Young Dong Kim, and H. Cheong, *Interference effect on Raman spectrum of graphene on SiO_2/Si*, Phys. Rev. B (2009) **80**, 125422.

7. X. Chen, X. Wang, and De Fang, *A review on C1s XPS-spectra for some kinds of carbon materials*, FULLERENES, NANOTUBES AND CARBON NANOSTRUCTURES (2020) **28**, 1048–1058.

8. R. Blume, D. Rosenthal, J.-P. Tessonnier, H. Li, A. Knop-Gericke, R. Schlogl, *Characterizing Graphitic Carbon with X-ray Photoelectron Spectroscopy: A Step-by-Step Approach*, ChemCatChem (2015) **7**, 2871.